

Article

NaTiO Nanoplatelets and Nanosheets Derived from a Modified Exfoliation Process for Use as a High Capacity Sodium-Ion Negative Electrode

Jesse S. Ko, Vicky V. T. Doan-Nguyen, Hyungseok Kim, Guillaume
Adolphe Muller, Andrew C. Serino, Paul S. Weiss, and Bruce S. Dunn

ACS Appl. Mater. Interfaces, **Just Accepted Manuscript** • DOI: 10.1021/acsami.6b10790 • Publication Date (Web): 20 Dec 2016

Downloaded from <http://pubs.acs.org> on December 20, 2016

Just Accepted

"Just Accepted" manuscripts have been peer-reviewed and accepted for publication. They are posted online prior to technical editing, formatting for publication and author proofing. The American Chemical Society provides "Just Accepted" as a free service to the research community to expedite the dissemination of scientific material as soon as possible after acceptance. "Just Accepted" manuscripts appear in full in PDF format accompanied by an HTML abstract. "Just Accepted" manuscripts have been fully peer reviewed, but should not be considered the official version of record. They are accessible to all readers and citable by the Digital Object Identifier (DOI®). "Just Accepted" is an optional service offered to authors. Therefore, the "Just Accepted" Web site may not include all articles that will be published in the journal. After a manuscript is technically edited and formatted, it will be removed from the "Just Accepted" Web site and published as an ASAP article. Note that technical editing may introduce minor changes to the manuscript text and/or graphics which could affect content, and all legal disclaimers and ethical guidelines that apply to the journal pertain. ACS cannot be held responsible for errors or consequences arising from the use of information contained in these "Just Accepted" manuscripts.

**ACS Publications**

ACS Applied Materials & Interfaces is published by the American Chemical Society.
1155 Sixteenth Street N.W., Washington, DC 20036
Published by American Chemical Society. Copyright © American Chemical Society.
However, no copyright claim is made to original U.S. Government works, or works
produced by employees of any Commonwealth realm Crown government in the course
of their duties.

Na₂Ti₃O₇ Nanoplatelets and Nanosheets Derived from a Modified Exfoliation Process for Use as a High Capacity Sodium-Ion Negative Electrode

Jesse S. Ko,[†] Vicky V. T. Doan-Nguyen,^{⊥,||} Hyung-Seok Kim,[†] Guillaume A. Muller,[†]

Andrew C. Serino,[†] Paul S. Weiss,^{†,‡,§} and Bruce S. Dunn^{*,†,§}

[†]Department of Materials Science and Engineering, University of California, Los Angeles, Los Angeles, CA 90095, United States

[‡]Department of Chemistry and Biochemistry, University of California, Los Angeles, Los Angeles, CA 90095, United States

[§]California NanoSystems Institute, University of California, Los Angeles, Los Angeles, CA 90095, United States

[⊥]California NanoSystems Institute, University of California, Santa Barbara, Santa Barbara, CA 93106, United States

^{||}Materials Research Laboratory, University of California, Santa Barbara, Santa Barbara, CA 93106, United States

ABSTRACT

The increasing interest in Na-ion batteries (NIBs) can be traced to sodium abundance, its low cost compared to lithium, and its intercalation chemistry being similar to that of lithium. We report that the electrochemical properties of a promising negative electrode material, Na₂Ti₃O₇, are improved by exfoliating its layered structure and forming 2D nanoscale morphologies, nanoplatelets and nanosheets. Exfoliation of Na₂Ti₃O₇ was carried out by controlling the amount of proton exchange for Na⁺ and then proceeding with the intercalation of larger cations such as methylammonium and propylammonium. An optimized mixture of nanoplatelets and nanosheets exhibited the best electrochemical performance in terms of high capacities in the range of 100 to 150 mAh g⁻¹ at high rates with stable cycling over several hundred cycles. These properties far exceed those of the corresponding bulk material, which is characterized by slow charge storage kinetics and poor long-term stability. The results reported in this study demonstrate that charge-storage processes directed at 2D morphologies of surfaces and few layers of sheets are an exciting direction for improving the energy and power density of electrode materials for NIBs.

Keywords: Na-ion battery, 2D materials, anode, nanomaterials, electrochemistry, high-rate

INTRODUCTION

The ubiquitous nature of electrochemical energy storage (EES) has led to improvements in areas ranging from grid reliability to vehicle electrification and portable electronics. The development of low-cost EES systems for the electric grid is particularly attractive because of the prospect of handling peak demand without the need to build additional generating capacity.^{1,2} Secondary batteries possess a number of desirable features for EES systems including scalability, pollution-free operation, high round-trip efficiency and flexible power and energy characteristics to meet different grid functions. Among the various battery technologies, Li-ion batteries (LIBs) have emerged as the most attractive one for grid storage since this technology outperforms competing battery technologies by a substantial margin.¹ The high energy density, safety and reliability demonstrated by LIBs for mobile applications are also beneficial for stationary energy storage and a number of grid demonstration projects are underway.²

There is, however, growing concern that the demand for lithium will impact the existing world reserves and its abundance will become an economic concern. For this reason, there is renewed interest in Na-ion batteries (NIBs) as there are ample reserves of sodium and its intercalation chemistry is similar to that of lithium.^{3–6} Some fundamental differences impede the immediate implementation of NIBs such as the larger ionic radius of Na⁺ (1.02 Å) compared to Li⁺ (0.76 Å), its mass (23 g mol⁻¹) is three times heavier than Li⁺ (6.9 g mol⁻¹), and the standard reduction potential (-2.71 V vs. S.H.E.) is slightly more positive compared to Li⁺ (-3.04 V vs. S.H.E.);³ these differences inevitably lead to lower energy densities and possibly lower power densities. Nonetheless, there have been several reports indicating that Na-ion insertion compounds can exhibit capacities of up to 150 mAh g⁻¹ for use as positive electrodes.^{3,6,7} It should be noted that the number of positive electrode materials that have been studied far outweighs the number of studies of negative electrode materials.^{7,8}

The two basic reversible approaches that have been developed for LIB negative electrodes, namely the use of alloying and intercalation reactions, have been extended to NIBs. Group 14 and 15 elements (metals and metalloids) are known to alloy with Na⁺, and Na alloys with P, Sb, and Sn lead to capacities in excess of 500 mAh g⁻¹, much greater than what can be achieved with commercial lithium negative electrodes based on graphite.⁹ However, the high volume expansion that occurs on alloying lithium also plagues sodium-based alloys, making these materials difficult to utilize for energy storage as the high volume expansion limits long-term cycling. Upon continuous charge-discharge cycles, alloy materials suffer from mechanical stress caused by volume expansion and repeated passivation of the electrolyte.⁸ Although intercalation compounds are not capable of storing as much capacity compared to that of alloying compounds, their limited volume expansion and overall stability upon repeated cycling make this a promising class of materials for negative electrodes.

Intercalation compounds based on metal oxides, in particular sodium titanates, are currently being studied as negative electrode materials for NIBs. These sodium titanates include

a variety of metastable and stable compounds (*i.e.*, $\text{Na}_2\text{Ti}_3\text{O}_7$, $\text{Na}_2\text{Ti}_6\text{O}_{13}$, $\text{NaTi}_3\text{O}_6(\text{OH})\cdot 2\text{H}_2\text{O}$, and lepidocrocite structures) that have low operating voltages *vs.* Na/Na^+ .^{10–14} With $\text{Na}_2\text{Ti}_3\text{O}_7$, the subject of this paper, Senguttuvan *et al.* first demonstrated that layered $\text{Na}_2\text{Ti}_3\text{O}_7$ can reach capacities of 200 mAh g^{-1} at relatively low potentials ($0.3 \text{ V vs. Na}/\text{Na}^+$), albeit at a slow charging rate ($C/25$).¹⁵ After this initial report, Rudola *et al.* and Pan *et al.* investigated several process-related parameters such as smaller particle size and ball-milling. This approach led to high capacities of approximately 190 mAh g^{-1} at slightly faster rates.^{14,16} However, one of the biggest limitations for this material is its long-term cycling performance where a capacity of 190 mAh g^{-1} decreases about 60% after 100 cycles.¹⁴ Moreover, there has yet to be any report where $\text{Na}_2\text{Ti}_3\text{O}_7$ exhibits rapid charge storage and retains high capacity.

The problem of capacity fade and slow kinetics can be traced to the bulk material properties of $\text{Na}_2\text{Ti}_3\text{O}_7$. First, micron-sized particles inherently face longer diffusion times throughout the structure due to longer diffusion path lengths. In addition, bulk $\text{Na}_2\text{Ti}_3\text{O}_7$ is predicted to undergo a moderate amount of volume expansion of 6% from Density Functional Theory (DFT) calculations.¹⁷ The repeated expansion and contraction of the structure may be an important factor that contributes to poor long-term cycling. For these reasons, we became interested in the question of whether these limitations can be overcome by changing the dimensionality of $\text{Na}_2\text{Ti}_3\text{O}_7$ from 3D to 2D, with the latter being in the form of nanoplatelets and nanosheets.

The extraordinary properties of graphene have led to renewed interest in a wide range of two-dimensional (2D) materials.¹⁸ When prepared as nanosheets, various transition metal oxides and chalcogenides can exhibit interesting modulation of their chemical and physical properties.^{19–22} Several synthesis strategies have been carried out to obtain 2D nanosheets such as liquid-phase exfoliation, mechanical exfoliation, thermal decomposition, direct chemical synthesis, and chemical vapor deposition.^{20,22–25} Among the various techniques, liquid-phase exfoliation offers a scalable process that has the potential to provide large quantities of dispersed nanosheets that can be processed using existing industrial techniques such as reel-to-reel manufacturing.²⁰

In the research reported here, we developed a liquid-phase exfoliation method that enabled us to obtain both 2D nanoplatelets and nanosheets. The motivation for evaluating nanoplatelets was based on the premise that few layers of sheets can provide for facile Na-ion intercalation compared to bulk materials. Furthermore, it is not clear whether a single layer nanosheet can store high levels of charge since there are a limited number of intercalation sites for Na-ions. By establishing a good understanding of the exfoliation process, we were able to control synthesis conditions and obtain both nanosheets and nanoplatelets. To achieve charge storage levels greater than 100 mAh g^{-1} , we show that a combination of both 2D nanoplatelets and nanosheets provides an optimized condition that offers rapid kinetics, high capacities for Na-ion charge storage, and a wider electrochemical voltage window.

2. MATERIALS AND METHODS

Synthesis of Na₂Ti₃O₇ Nanoplatelets and PA/Ti₃O₇ Nanosheets. Bulk Na₂Ti₃O₇ (2 mmol) was prepared by mixing stoichiometric amounts of anatase titanium(IV) oxide (Sigma-Aldrich, 99.9%) and sodium carbonate (Sigma-Aldrich, 99.9%) and subsequently heating in air at 800 °C for 40 h with intermediate re-grinding. The first step in the exfoliation process involved proton exchange for Na-ions present in the layered compound Na₂Ti₃O₇. This process was carried out by completely dissolving ~0.3 g of Na₂Ti₃O₇ powder in 25 mL of 1M hydrochloric acid and stirring at 1000 rpm for 24 h. The partially protonated form [H_xNa_{2-x}]Ti₃O₇ was then centrifuged at 5000 rpm. The remaining hydrochloric acid was then decanted and the resultant [H_xNa_{2-x}]Ti₃O₇ powder was re-suspended in 11 mL of methylamine (80 mol methylamine per mol of [Ti₃O₇]²⁻) solution (Sigma-Aldrich, 40 wt.% in H₂O) and stirred at 1000 rpm for 6 days at 60 °C. Next, the methylamine-reacted mixture [MA_yH_{x-y}Na_{2-x}]Ti₃O₇ was centrifuged at 5000 rpm and re-suspended with 8 mL of propylamine (80 mol propylamine per mol of [Ti₃O₇]²⁻) solution (Sigma-Aldrich, ≥99.9%) after decanting the reacted methylamine solution. This propylamine mixture [PA_yH_{x-y}Na_{2-x}]Ti₃O₇ was then stirred at 1000 rpm for 6 days at 60 °C. It was important to seal the container tightly with Teflon tape due to the high volatility of this solvent. This 8 mL solution containing [PA_yH_{x-y}Na_{2-x}]Ti₃O₇ was then washed with de-ionized water and centrifuged at 5000 rpm. The supernatant was decanted and the sedimented particles were re-suspended with de-ionized water and subjected to ultrasonication for 5 minutes to exfoliate [PA_yH_{x-y}Na_{2-x}]Ti₃O₇. After sonication, by adjusting centrifuge conditions, we were able to obtain solutions comprised solely of nanoplatelets (Na₂Ti₃O₇ NP) and nanosheets (PA/Ti₃O₇ NS) or mixtures of both (Na₂Ti₃O₇ NP-NS). These solutions give large quantities of dispersed nanosheets that enable scalable processing using industrial techniques.^{20,22}

Materials Characterization. Transmission electron microscopy (TEM) images were taken with an FEI Technai T12 TEM (120 keV) using a carbon-coated copper grid as a substrate. X-ray diffraction (XRD) was carried out by using a Rigaku Miniflex II diffractometer. X-ray pair distribution function analysis was performed at the Advanced Photon Source 11-ID-B at Argonne National Laboratory. Total scattering experiments were performed using a $\lambda = 0.2112 \text{ \AA}$ (~58 keV) X-ray source with a Perkin-Elmer amorphous Si-based 2D detector, which allows for rapid acquisition.²⁶ To calibrate the experimental geometry of the measurements, a N.I.S.T.-traceable CeO₂ (Standard Reference Material[®] 674b) standard powder was used. The sample-to-detector distance for synchrotron XRD was calibrated to 952.276 mm. Azimuthal angle analysis was performed with NIKA.²⁷ The sample-to-detector distance for PDF experiments were calibrated to 181.574 mm. The 2D data were integrated using Fit2D.²⁸ Pair distribution functions (PDFs), $G(r)$, were calculated from the sine Fourier transform of the product $q(S(q)-1)$ in which $S(q)$ is the structure factor. PDFs were generated with a $q_{\text{max}} = 24 \text{ \AA}^{-1}$ using PDFgetX2.²⁹ X-ray Photoelectron Spectroscopy (XPS) measurements were collected using an AXIS Ultra DLD instrument (Kratos Analytical Inc., Chestnut Ridge, NY). All measurements were conducted under ultrahigh vacuum (10^{-9} torr) using a monochromatic Al K α X-ray source

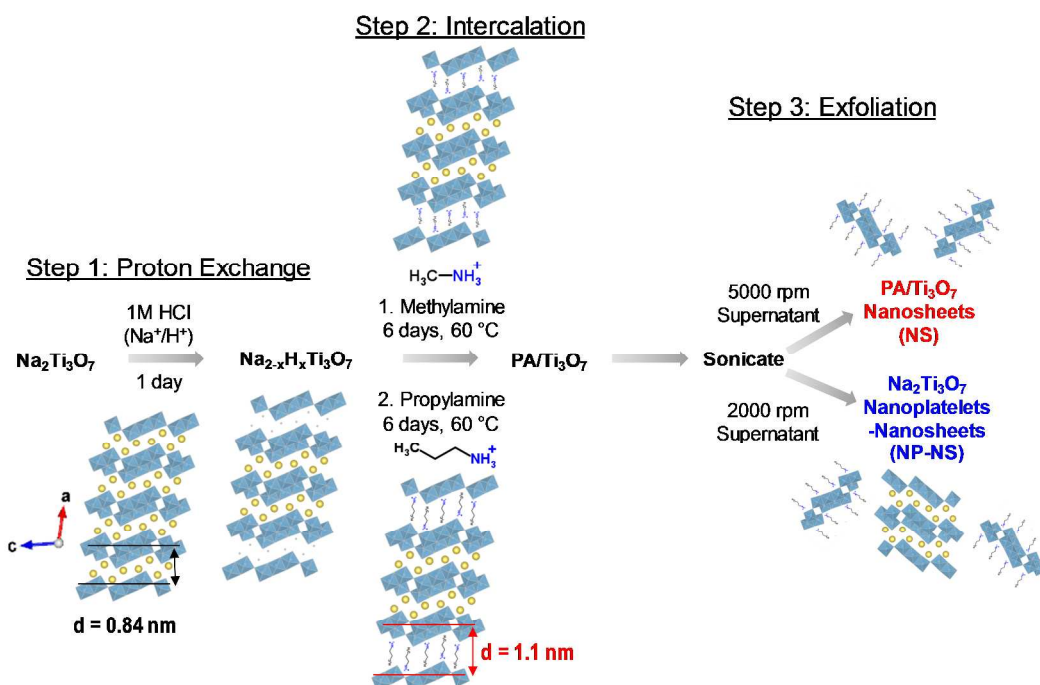
(20 mA, 14 kV) with a 200 μm circular spot size. XPS spectra for all samples were acquired at 300 W (20 mA, 15 kV), with a pass energy of 160 eV for collecting atomic compositions (survey scans can be found in Figure S10) and a pass energy of 20 eV for collecting high-resolution spectra. Each scan had a dwell time of 200 ms where each element was swept 20 times. Atomic force microscopy (AFM) was performed in tapping mode using a Bruker Dimension Icon system. Details of the sample preparation can be found in the Supporting Information.

Electrochemical Characterization. Cyclic voltammetry experiments were carried out in a three-electrode flooded cell using a BioLogic VMP-3 Potentiostat. All experiments were conducted in an argon-filled glovebox with moisture and oxygen levels <1 ppm. The electrolyte solution used was 1M sodium perchlorate (NaClO_4 , Alfa-Aesar, 99.8% anhydrous) in a 95:5 (v:v) mixture of propylene carbonate ($\text{C}_4\text{H}_6\text{O}_3$, Alfa-Aesar, 98%) and fluoroethylene carbonate ($\text{C}_3\text{H}_3\text{FO}_3$, Alfa-Aesar, 98%) and sodium metal foils were used as both the counter and reference electrodes. The working electrode was prepared by drop-casting a 2 g L^{-1} solution of either PA/ Ti_3O_7 NS, $\text{Na}_2\text{Ti}_3\text{O}_7$ NP or the mixed nanoplatelet-nanosheet system ($\text{Na}_2\text{Ti}_3\text{O}_7$ NP-NS) onto an O_2 plasma cleaned stainless steel current collector ($1 \text{ cm} \times 1 \text{ cm}$). These thin-film electrodes contained neither binder nor carbon as this arrangement enables one to determine the fundamental electrochemical properties of the electrode material.³⁰ After drop-casting, the electrodes were heated at 120°C under vacuum overnight to remove excess solvent and also to provide sufficient binding to the current collector. The amount of active material on the electrodes, on the order of $40 \mu\text{g cm}^{-2}$, was confirmed using a Cahn C-31 microbalance. Cyclic voltammetry and galvanostatic cycling were performed using cutoff voltages of 2.5 and 0.1 V vs. Na^+/Na . The sweep rates for the former were between 1 and 100 mV s^{-1} . The current densities used for galvanostatic cycling ranged from 100 to 2000 mAh cm^{-2} . Based on the capacity of the $\text{Na}_2\text{Ti}_3\text{O}_7$ NP-NS materials, we estimate that 100 mA cm^{-2} corresponds to 1C.

RESULTS AND DISCUSSION

Preparation of Nanoplatelets and Nanosheets. Several reports have shown that liquid-phase exfoliation of layered metal oxides is an efficient method for obtaining 2D nanosheets.^{19,20,22} In our study, two different nanoscale morphologies of interest in this project, titanate nanosheets (PA/ Ti_3O_7 NS) and sodium titanate nanoplatelets ($\text{Na}_2\text{Ti}_3\text{O}_7$ NP), were obtained by modifying a liquid-phase exfoliation process reported by Miyamoto *et al.*³¹ The synthesis is based on intercalating large cations between slabs of $[\text{Ti}_3\text{O}_7]^{2-}$ sheets from the parent layered compound, $\text{Na}_2\text{Ti}_3\text{O}_7$, and then separating by ultrasonication. The key steps that enable us to obtain both PA/ Ti_3O_7 NS and $\text{Na}_2\text{Ti}_3\text{O}_7$ NP are through partial proton exchange of the Na-ions in $\text{Na}_2\text{Ti}_3\text{O}_7$ and varying the centrifugation speed. Energy dispersive spectroscopy measurements tracking the amount of sodium based on duration of proton exchange are shown in Figure S1 and the corresponding XRD patterns in Figure S2. Upon proton exchange, the organic base methylamine is intercalated into the interlayer region of the $[\text{Ti}_3\text{O}_7]^{2-}$ sheets. The protonated sheets then work as a Brönsted acid and react with methylamine,³² forming an intercalation compound with now positively charged methylammonium (MA/ Ti_3O_7). The methylammonium

intercalation compound is then ion-exchanged with positively charged propylamine to form a propylammonium (PA^+) intercalated compound ($\text{PA}/\text{Ti}_3\text{O}_7$).^{31,33} Upon sonication, only those layers that were inserted with the larger PA^+ ions are exfoliated as single layer nanosheets due to weak sheet-to-sheet interaction. The remaining compound is in the form of nanoplatelets. As illustrated in Scheme 1, this solution is then centrifuged at 5000 rpm to isolate pure $\text{PA}/\text{Ti}_3\text{O}_7$ NS in the supernatant. The amount of PA^+ ions in $\text{PA}/\text{Ti}_3\text{O}_7$ was previously reported to be 0.56 mol per 1 mol of $[\text{Ti}_3\text{O}_7]^{2-}$ with the remainder of the negatively charged sheets compensated by protons.³¹ With a slower centrifugation speed of 2000 rpm, a mixture of nanoplatelets and nanosheets ($\text{Na}_2\text{Ti}_3\text{O}_7$ NP-NS) are obtained where the concentration of nanoplatelets is ~35%.



Scheme 1. Exfoliation flowchart for obtaining propylammonium Ti_3O_7 nanosheets ($\text{PA}/\text{Ti}_3\text{O}_7$ NS) and mixed nanoplatelets and nanosheets of $\text{Na}_2\text{Ti}_3\text{O}_7$ ($\text{Na}_2\text{Ti}_3\text{O}_7$ NP-NS) by altering centrifugation and ion exchange conditions.

We used differential centrifugation, a technique commonly applied with biological systems to isolate cellular components, to control the relative concentrations of nanoplatelets and nanosheets in the $\text{Na}_2\text{Ti}_3\text{O}_7$ NP-NS solution.³⁴ This preparation method is described in detail in the Supporting Information and an illustration of this process is shown in Figure S4. More importantly, centrifuging the solution of $\text{Na}_2\text{Ti}_3\text{O}_7$ NP-NS at 1000 rpm resulted in the isolation of $\text{Na}_2\text{Ti}_3\text{O}_7$ NP. That is, by adjusting centrifuge conditions, we were able to obtain solutions comprised solely of $\text{PA}/\text{Ti}_3\text{O}_7$ NS or nearly entirely of $\text{Na}_2\text{Ti}_3\text{O}_7$ NP. These isolated systems enable us to obtain control samples for the electrochemical experiments (*vide infra*). The X-ray diffraction (XRD) patterns (Figure S5a) and electrochemical characteristics (Figures S5b–d) of these controls are detailed in the Supporting Information. The best electrochemical results were

achieved with a combination of nanoplatelets and nanosheets; thus, the focus of this report is on the $\text{Na}_2\text{Ti}_3\text{O}_7$ NP-NS materials.

Structural and Chemical Characterization. Transmission electron microscopy (TEM) images of bulk $\text{Na}_2\text{Ti}_3\text{O}_7$, $\text{PA/Ti}_3\text{O}_7$ NS, and $\text{Na}_2\text{Ti}_3\text{O}_7$ NP-NS are presented in Figure 1. The bulk particles appear darker and more opaque compared to nanosheets and nanoplatelets since the larger non-exfoliated particles are thicker. On the other hand, $\text{PA/Ti}_3\text{O}_7$ NS appear nearly transparent given that the sheet thickness is on the order of 1.2 nm, as confirmed by atomic force microscopy (Figure S7); this thickness resembles the depth of a single slab of a $[\text{Ti}_3\text{O}_7]^{2-}$ building block (0.98 nm).³¹ In Figure 1c, $\text{Na}_2\text{Ti}_3\text{O}_7$ NP within a bed of transparent $\text{PA/Ti}_3\text{O}_7$ NS can be seen. The widths of both the nanosheets and nanoplatelets range from 100 to 200 nm and their lengths extend from several hundred nanometers to microns.

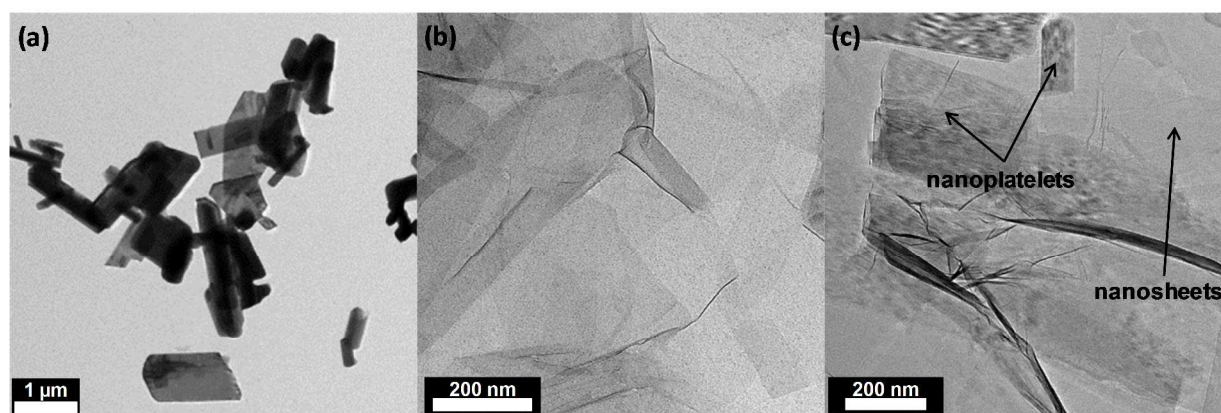


Figure 1. Transmission electron microscopy images of (a) bulk $\text{Na}_2\text{Ti}_3\text{O}_7$ (b) $\text{PA/Ti}_3\text{O}_7$ nanosheets, (c) mixed nanoplatelets and nanosheets of $\text{Na}_2\text{Ti}_3\text{O}_7$.

A series of X-ray studies were performed to characterize the structural and chemical properties of the nanoscale morphologies. First, XRD was used to verify the phase of bulk $\text{Na}_2\text{Ti}_3\text{O}_7$, $\text{PA/Ti}_3\text{O}_7$ NS, and $\text{Na}_2\text{Ti}_3\text{O}_7$ NP-NS (Figure 2a). These materials were compared to the bulk ($\text{P2}_1/\text{m}$) structure in which $a = 8.565 \text{ \AA}$, $b = 3.802 \text{ \AA}$, $c = 9.128 \text{ \AA}$, and $\beta = 101.5890^\circ$ (JCPDS 72-0148). Bulk $\text{Na}_2\text{Ti}_3\text{O}_7$ synthesized via solid state reaction agrees with referenced indices.³⁵ After exfoliation, $\text{PA/Ti}_3\text{O}_7$ NS exists as a purely isolated morphology while $\text{Na}_2\text{Ti}_3\text{O}_7$ NP-NS exists as two separate morphologies, as shown in Figure 2a. $\text{PA/Ti}_3\text{O}_7$ NS and $\text{Na}_2\text{Ti}_3\text{O}_7$ NP-NS both exhibit preferential orientation in the $(h00)$ plane since the re-stacking of the sheets leads to alignment in this direction. For pure $\text{PA/Ti}_3\text{O}_7$ NS, the (100) reflection shifts to lower 2θ from 10.5° to 8.0° (2θ), which corresponds to an increased d -spacing from 0.8 to 1.1 nm. The increased d -spacing is consistent with previous exfoliation results reported by Zhang *et al.*³⁶ and Miyamoto *et al.*³¹ where both reports consistently found that $[\text{Ti}_3\text{O}_7]^{2-}$ sheets reassemble and are separated by the larger positively charged PA^+ cation that acts as a counter charge to the negatively charged sheets.³¹ The (100) reflection is then accompanied by a weaker (200) reflection with $d(200)$ being 0.54 nm. For $\text{Na}_2\text{Ti}_3\text{O}_7$ NP-NS, the same (100) as that observed for $\text{PA/Ti}_3\text{O}_7$ NS is evident as is the (100) reflection for bulk $\text{Na}_2\text{Ti}_3\text{O}_7$. As a result of partial ion

exchange, Na^+ remains between the stacked layers and a characteristic peak for nanoplatelets at 10.5° (2θ) is observed. The ratio of the concentration of nanoplatelets to nanosheets in $\text{Na}_2\text{Ti}_3\text{O}_7$ NP-NS was estimated to be 9:16 by taking the ratio of the integrated intensities of the two most intense XRD reflections, one at 10.5° (2θ) for the nanoplatelets, and the other at 8.0° (2θ) for the nanosheets. The estimated number of layers and crystallite thicknesses for all samples using X-ray diffraction are tabulated in Table S1.³⁷

Synchrotron X-ray scattering and pair distribution functions (PDFs) of bulk and $\text{Na}_2\text{Ti}_3\text{O}_7$ NP-NS were also studied to compare their morphologies. The X-ray scattering image of $\text{Na}_2\text{Ti}_3\text{O}_7$ NP-NS is shown in the graphic in Figure 2b. The PA^+ interspersed layers can be seen in the decrease in q for the (100) planes at 0.59 \AA^{-1} (d -spacing = 10.7 \AA) as consistently evidenced from benchtop XRD ($\lambda = 1.54 \text{ \AA}$). With increased q resolution, we observed additional ($h00$) peaks at $q = 1.16, 1.72, 2.51, 3.04 \text{ \AA}^{-1}$ for $h = 2, 3, 4, 5$, respectively. These correspond to d -spacings of $5.46, 3.67, 2.51, 2.06 \text{ \AA}$ (Figure S8). For bulk $\text{Na}_2\text{Ti}_3\text{O}_7$, the (100) peak is maintained at $q = 0.75 \text{ \AA}^{-1}$ (d -spacing = 8.38 \AA) in agreement with the calculated XRD pattern. The diffraction pattern captures the morphological anisotropy of the 2D nanoplatelets shown in the azimuthal scans (Figure S9). The bulk PDF matches that of the calculated PDF of the monoclinic $\text{P2}_1/\text{m}$ structure in Figure 2b. Moreover, the signal from $\text{Na}_2\text{Ti}_3\text{O}_7$ NP-NS PDF is quickly damped by $r \approx 10 \text{ \AA}$ due to smaller particle size.³⁸ The $G(r)$ peak centers corresponding to bond distances of Ti-O ($1.95 \text{ \AA}, 2.28 \text{ \AA}, 3.75 \text{ \AA}, 4.33 \text{ \AA}, 7.18 \text{ \AA}, 8.90 \text{ \AA}$), Ti-Ti ($3.17 \text{ \AA}, 6.23 \text{ \AA}$), Na-Ti ($4.97 \text{ \AA}, 8.15 \text{ \AA}$), and Na-O ($2.62 \text{ \AA}, 7.57 \text{ \AA}$) remain unchanged between the bulk and the NP-NS samples. However, the peak widths are narrower for the bulk sample as compared to the NP-NS sample. The Na-Ti bond at 9.04 \AA is damped significantly for the NP-NS sample relative to that of the bulk sample as a result of the decreased coherence length in the nanomaterial. The results attained from synchrotron X-ray scattering and PDFs show that the nanostructure correlation length agrees with the interlayer spacing of the nanosheets as confirmed by X-ray diffraction.

X-ray photoelectron spectroscopy (XPS) was used to determine the chemistry of the interlayers before and after the exfoliation process. XPS spectra for bulk $\text{Na}_2\text{Ti}_3\text{O}_7$, $\text{PA/Ti}_3\text{O}_7$ NS and $\text{Na}_2\text{Ti}_3\text{O}_7$ NP-NS are shown in Figures 2c–d. The Na 1s and N 1s characteristic peaks provide both quantitative and qualitative information about the amount of Na^+ and $-\text{C-NH}_3^+$. In addition, each Na 1s and N 1s spectrum was high-resolution fitted to obtain a more accurate measure of the amount of Na^+ and $-\text{C-NH}_3^+$ present; the high-resolution XPS spectra are shown in Figures S11 and S12 for N 1s and Na 1s, respectively. The corresponding chemical environment based on the fittings is also listed in the corresponding figures and are consistent with what is reported in literature for both the N 1s and Na 1s binding energies.^{39–42} As expected, the N 1s spectrum of bulk $\text{Na}_2\text{Ti}_3\text{O}_7$ shows no indication of $-\text{C-NH}_3^+$ ($\sim 401 \text{ eV}$) whereas a peak is evident for the $\text{PA/Ti}_3\text{O}_7$ NS due to the existence of PA^+ ions in between the $[\text{Ti}_3\text{O}_7]^{2-}$ sheets. As for the Na 1s spectrum, the intense Na 1s peak for bulk $\text{Na}_2\text{Ti}_3\text{O}_7$ (1071 eV) decreases significantly for $\text{PA/Ti}_3\text{O}_7$ NS. For $\text{Na}_2\text{Ti}_3\text{O}_7$ NP-NS, a strong Na 1s peak is present due to the

remaining Na-ions in between the layers from the partial exfoliation process. Taken together, the combination of both the N 1s and Na 1s XPS spectra shows that the concentration of Na^+ and $-\text{C-NH}_3^+$ differs dramatically depending on whether we have NS or NP. Using the results from the scans in Figures S10–S12, we obtained atomic percentages of Na 1s and N 1s for bulk $\text{Na}_2\text{Ti}_3\text{O}_7$, PA/ Ti_3O_7 NS, $\text{Na}_2\text{Ti}_3\text{O}_7$ NP-NS, and $\text{Na}_2\text{Ti}_3\text{O}_7$ NP-NS after cycling in 1M NaClO_4 in PC:FEC (Table S2). To summarize, before exfoliation, the ratio of the atomic percentage of Na^+ to $-\text{C-NH}_3^+$ is 1:0 (bulk $\text{Na}_2\text{Ti}_3\text{O}_7$). After exfoliation, the ratio of the atomic percentage of Na^+ to $-\text{C-NH}_3^+$ for PA/ Ti_3O_7 NS was measured to be 1:60. For the material containing both NS and NP, the ratio of the atomic percentage of Na^+ to $-\text{C-NH}_3^+$ is 1:6.6.

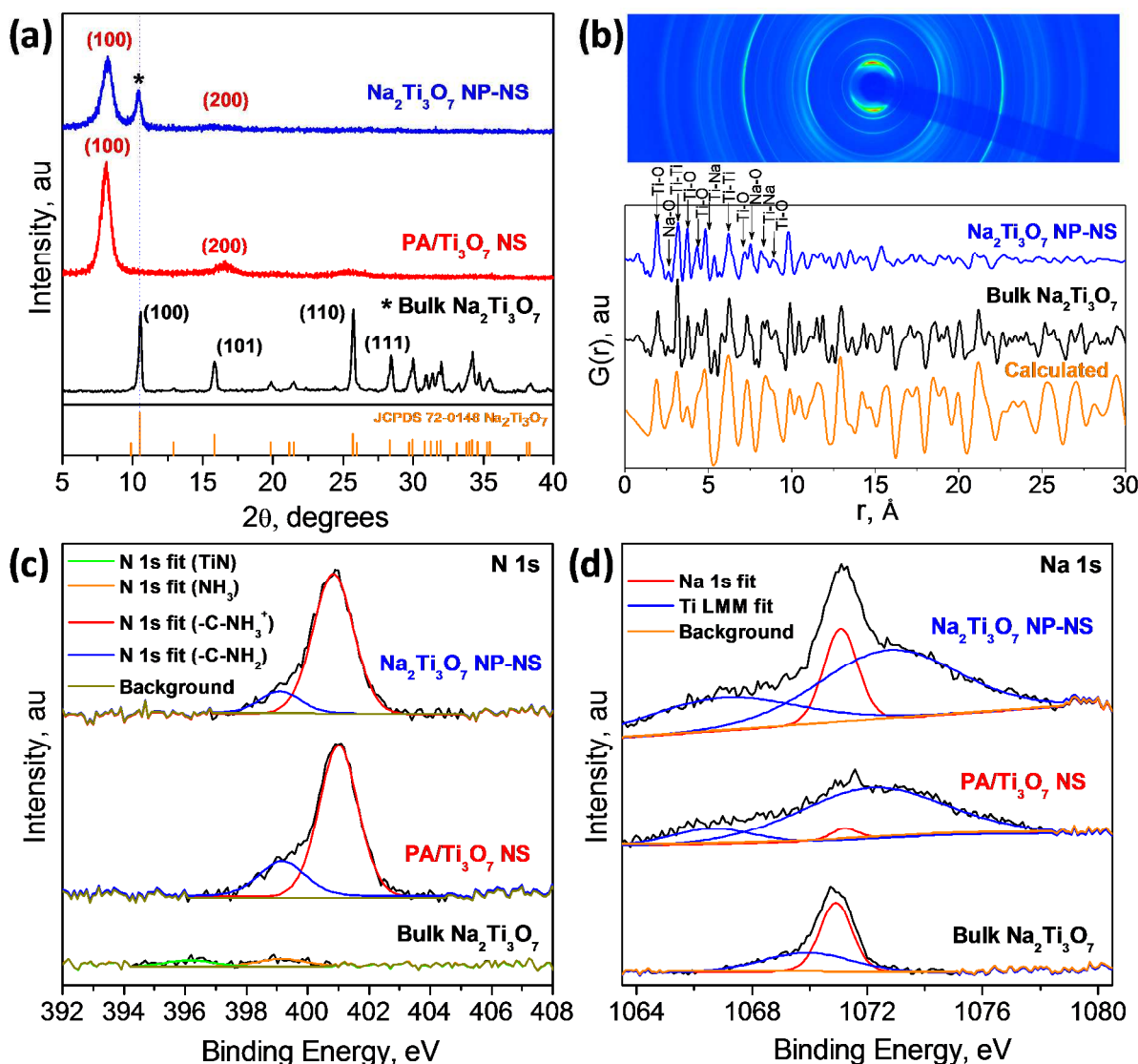


Figure 2. $\text{Na}_2\text{Ti}_3\text{O}_7$, PA/ Ti_3O_7 nanosheets, and mixed nanoplatelets and nanosheets of $\text{Na}_2\text{Ti}_3\text{O}_7$. (a) X-ray diffraction patterns obtained from the modified exfoliation process. (b) Total X-ray scattering where evidence of preferential orientation for the ($h00$) reflection is shown. X-ray photoelectron spectra from the (c) N 1s and (d) Na 1s core-levels.

Electrochemical Properties. Cyclic voltammetry measurements are able to identify the electrochemical behavior of $\text{Na}_2\text{Ti}_3\text{O}_7$ NP-NS in comparison to the control samples of pure PA/ Ti_3O_7 NS and $\text{Na}_2\text{Ti}_3\text{O}_7$ NP. The redox peaks for the nanoplatelets and nanosheets occur at decidedly different potentials. Individual CVs of pure PA/ Ti_3O_7 NS and isolated $\text{Na}_2\text{Ti}_3\text{O}_7$ NP as control samples are shown in Figure S5. For pure $\text{Na}_2\text{Ti}_3\text{O}_7$ NP, only low potential redox peaks in the cyclic voltammograms (CVs) between 0.1 and 0.5 V vs. Na/Na⁺ appear; this behavior resembles the electrochemical properties of bulk $\text{Na}_2\text{Ti}_3\text{O}_7$, as shown in Figure S5b.^{14–16} In comparison, PA/ Ti_3O_7 NS (inset in Figure 3a) exhibit energy storage at higher voltages between 0.5 and 2.5 V (vs. Na/Na⁺). Thus, specific redox peaks associated with $\text{Na}_2\text{Ti}_3\text{O}_7$ NP occur at 0.18 and 0.26 V vs. Na/Na⁺ for the cathodic and anodic peaks, respectively, whereas the cathodic and anodic peaks occur, respectively, at 1.1 and 1.2 V vs. Na/Na⁺ for PA/ Ti_3O_7 NS.

Combining the energy storage properties of NP and NS offers the opportunity to achieve energy storage by facile Na-ion diffusion with an expanded electrochemical window ranging from 0.1 to 2.5 V vs. Na/Na⁺. As illustrated in Figure 3a, the electrochemical signature for $\text{Na}_2\text{Ti}_3\text{O}_7$ NP-NS consists of two coupled redox peaks, one from the nanoplatelet morphology and the other from the nanosheets. Cyclic voltammograms swept from 1 to 20 mV s^{−1} are shown in Figure S13a. In addition to a widened electrochemical window, a key feature that distinguishes $\text{Na}_2\text{Ti}_3\text{O}_7$ NP-NS as a prospective anode material for NIBs is its fast charge-storage properties and high capacity for sodium.^{13,14,16,43} The rate capability and capacity of $\text{Na}_2\text{Ti}_3\text{O}_7$ NP-NS compared to pure PA/ Ti_3O_7 NS are shown by the sweep rate experiments in Figure 3b. The thin-film electrodes used in these experiments utilized low amounts of active material (~40 μg cm^{−2}) but contained neither binder nor carbon in order to assess the fundamental electrochemical properties associated with the different nanoscale morphologies. For $\text{Na}_2\text{Ti}_3\text{O}_7$ NP-NS, a capacity of 150 ± 5 mAh g^{−1} is achieved at a rate of 1 mV s^{−1} and 70% of that capacity (102 ± 7 mAh g^{−1}) is retained at an order of magnitude faster rate (10 mV s^{−1}). In contrast, PA/ Ti_3O_7 NS reach a maximum capacity of approximately 16 ± 7 mAh g^{−1} at 1 mV s^{−1}.

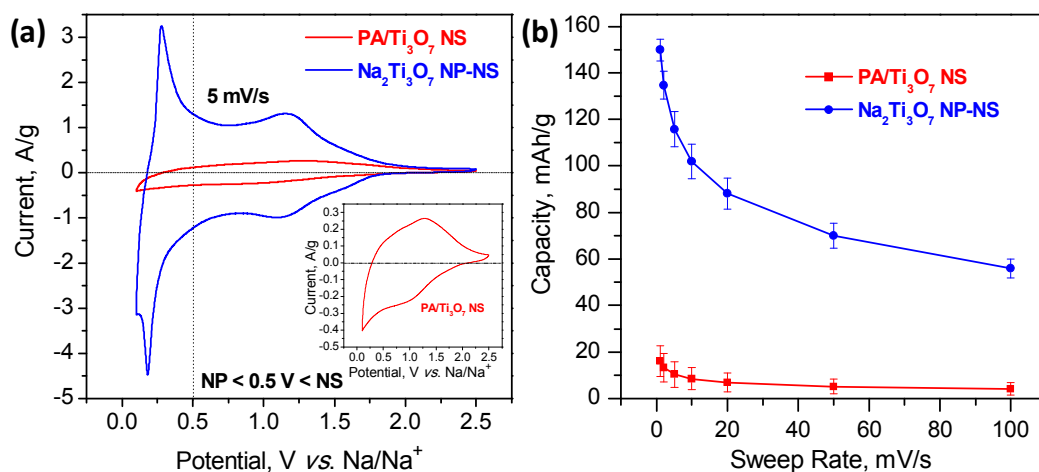


Figure 3. (a) Cyclic voltammograms of mixed nanoplatelets and nanosheets of Na₂Ti₃O₇ and PA/Ti₃O₇ nanosheets cycled at 5 mV s⁻¹ from 0.1 to 2.5 V vs. Na/Na⁺ and (b) corresponding rate capability (capacity vs. sweep rate).

Constant current measurements were also used to assess the charge storage properties of Na₂Ti₃O₇ NP-NS. On the first cycle, there is irreversible sodium loss from the formation of a solid electrolyte interphase (SEI) layer (Figure S14). Thereafter the galvanostatic charge-discharge curves stabilize as shown in Figure 4a. A significant feature of the discharge curves is that there are no distinct horizontal plateaus and the sloping voltage transients indicate single phase behavior.⁴⁴ The derivative dQ/dV plots (Figure S15) always show redox peaks at the low potentials, consistent with the peak positions shown from cyclic voltammetry (Figure 3a). When cycled at 1C (100 mA cm⁻²), the Na₂Ti₃O₇ NP-NS material stores nearly 160 mAh g⁻¹. As the charge-discharge rates are increased further, Na₂Ti₃O₇ NP-NS retains much of this high capacity and at a rate of 10C (1000 mA cm⁻²), this material stores 110 mAh g⁻¹. In addition to the high capacities, coulombic efficiencies higher than 95% were achieved. As shown in Figure 4c, the material exhibits excellent cycling stability, maintaining a capacity of 110 mAh g⁻¹ for some 300 cycles at 500 mA cm⁻². Although nanoscale materials have demonstrated enhanced properties for a number of systems, a contributing factor here for the improved electrochemical behavior may be the continuous decrease in potential (Figure 4a) associated with pseudocapacitive charge storage.^{44,45} To complement these thin film electrode studies, we carried out galvanostatic measurements using standard electrodes prepared with exfoliated Na₂Ti₃O₇ NP-NS (1 mg cm⁻² loading) to which carbon and binder were added. The results presented in Figure S16 show that these electrodes have poorer rate capability compared to the thin film electrodes (Figure 4a,b). However, in comparison to electrodes prepared with bulk Na₂Ti₃O₇, the performance is decidedly better (Figure S16b), underscoring the improvement in electrochemical properties by using these 2D materials.

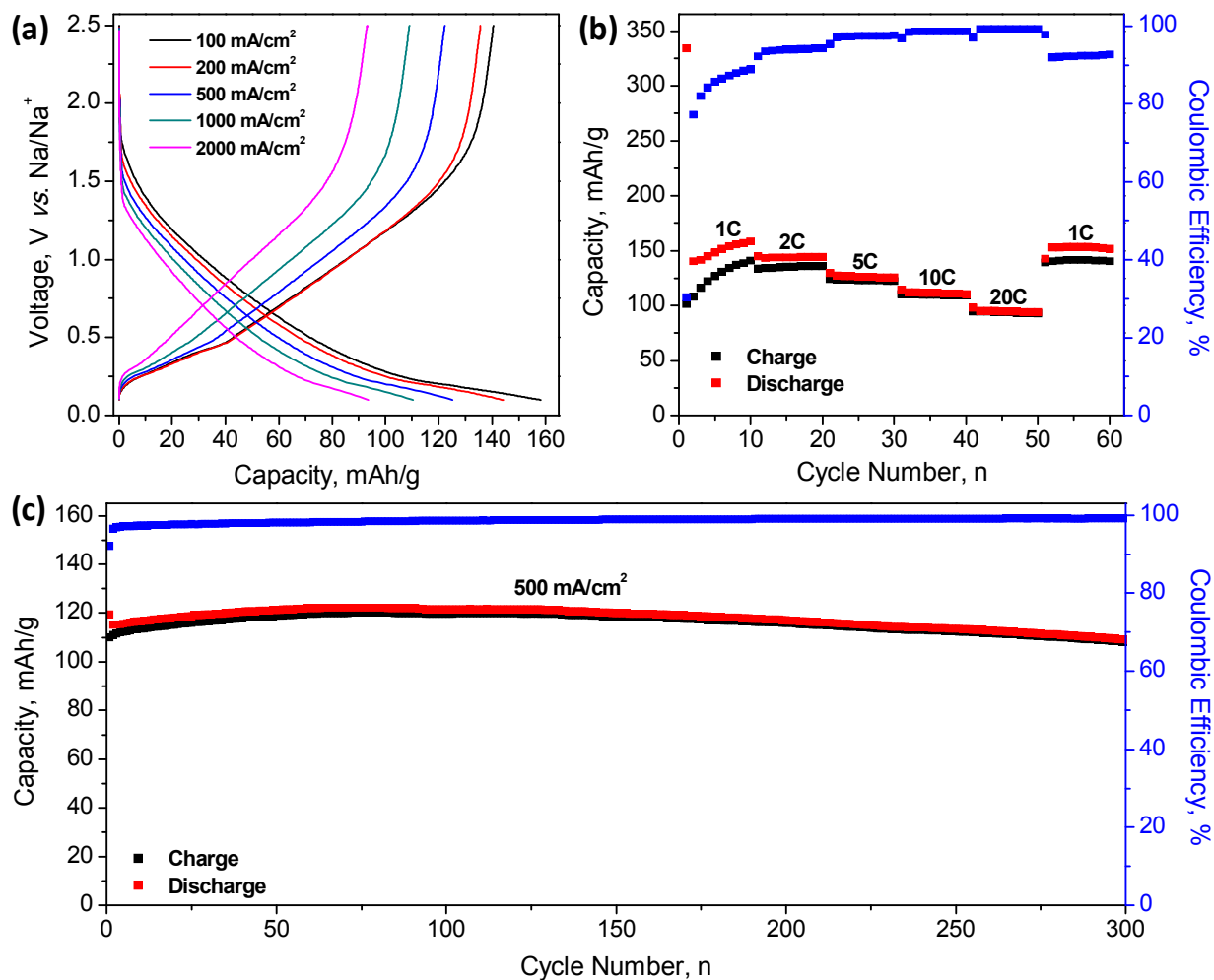


Figure 4. (a) 10th cycle galvanostatic charge-discharge curves of mixed nanoplatelets and nanosheets of $\text{Na}_2\text{Ti}_3\text{O}_7$ cycled at current densities between 100 and 2000 mA/cm^2 . (b) Capacity and coulombic efficiency measured from galvanostatic cycling at current densities between 100 and 2000 mA/cm^2 ; 1C is estimated as 100 mA/cm^2 . (c) Long-term cycling at 500 mA/cm^2 of mixed nanoplatelets and nanosheets of $\text{Na}_2\text{Ti}_3\text{O}_7$ for 300 cycles.

Kinetic Analysis. The charge-storage mechanisms for the two nanoscale morphologies, nanoplatelets and nanosheets, were analyzed for the different potential regimes. In this analysis, the peak current in the cyclic voltammetry experiment is determined as a function of sweep rate. The peak current (i) follows a power law relationship

$$i = av^b, \quad (1)$$

where a is a constant and v is the sweep rate. The b -value can change from 0.5, which is indicative of semi-infinite diffusion to a value of 1, indicating a capacitor-like process.⁴⁶ This b -value is obtained by determining the slope of $\log(i)$ vs. $\log(v)$ as shown for $\text{Na}_2\text{Ti}_3\text{O}_7$ NP and PA/ Ti_3O_7 NS in Figure 5a. At sweep rates ranging from 1 to 20 mV/s , the b -values for the cathodic peaks associated with the nanoplatelets (0.18 V vs. Na/Na^+) and nanosheets at (1.1 V vs.

Na/Na⁺) are calculated to be 0.7 and 1, respectively. The b -values for the anodic peaks associated with nanoplatelets and nanosheets are shown in Figures S13b,c, respectively. A value of $b=0.7$ for the peak at 0.18 V suggests that there is a significant diffusion contribution to the current, which is expected because these peaks are associated with Na⁺ insertion in Na₂Ti₃O₇ and the accompanying redox reactions. At 1.1 V, the $b = 1$ value is representative of a surface capacitive process, as expected for a nanosheet. These results establish that there are two different modes of charge storage for these different nanoscale morphologies.

The b -value analysis can be extended further to determine the relative contribution for each of the charge storage processes in Na₂Ti₃O₇ NP-NS materials. In this analysis, the current at a given potential has contributions from both capacitive and diffusion-controlled processes and is written as:⁴⁷

$$i(V) = k_1 v^{1/2} + k_2 v \quad (2)$$

Solving for the values of k_1 and k_2 at a given potential enables one to distinguish between currents that are related to semi-infinite diffusion and those that have capacitor-like kinetics. Figure 5b shows the capacitive contribution to the overall charge storage mechanism. The results are consistent with the b -values described above. Most of the diffusion contributions occur at potentials less than 0.5 V (vs. Na/Na⁺) where it is expected that Na⁺ will be inserted into the layers of the Na₂Ti₃O₇ NP, while capacitor-like behavior occurs at potentials above 0.9 V (vs. Na/Na⁺) where the nanosheets are found to have their contribution.

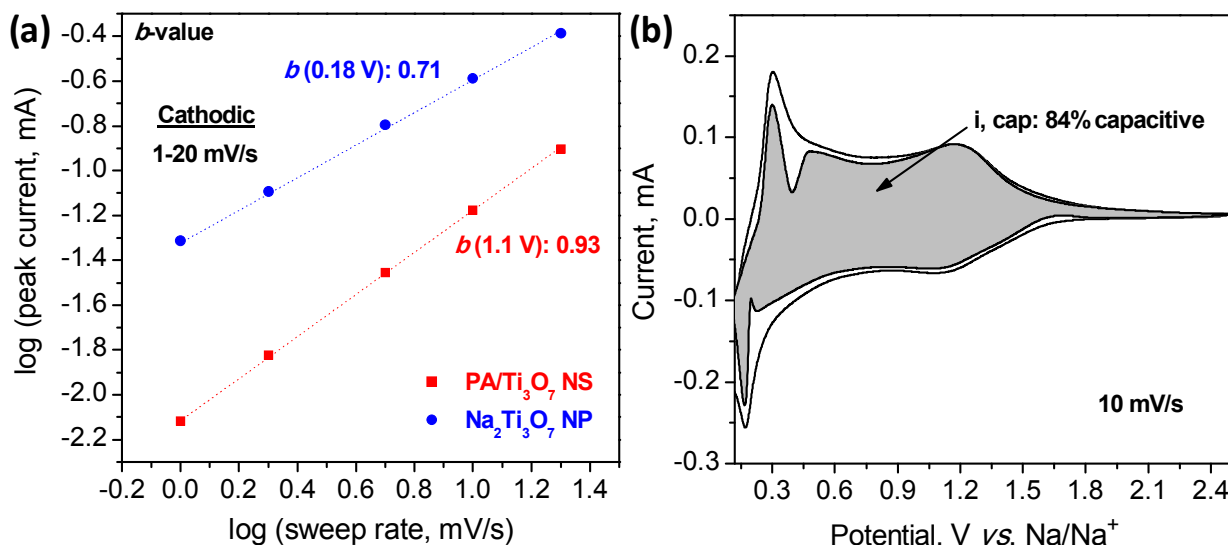


Figure 5. (a) Determination of the b -value using the peak current relationship to sweep rate (1 to 20 mV s⁻¹). (b) Cyclic voltammogram of mixed nanoplatelets and nanosheets of Na₂Ti₃O₇ showing 84% capacitive contribution when cycled at 10 mV s⁻¹.

Electrochemical Ion-Exchange. An interesting feature noticed for the $\text{Na}_2\text{Ti}_3\text{O}_7$ NP-NS materials is the increase in capacity with continued cycling. This capacity increase is shown in Figure 6a for cyclic voltammetry experiments when the potential is cycled between 0.1 and 2.5 V vs. Na/Na^+ . After several cycles, a pair of cathodic and anodic peaks appear at 0.18 and 0.26 V, respectively, with a concomitant appearance of an additional pair of cathodic and anodic peaks appearing at 1.1 V and 1.2 V. As discussed above, the low potential peaks mirror the behavior of bulk $\text{Na}_2\text{Ti}_3\text{O}_7$ and are attributed to the $\text{Na}_2\text{Ti}_3\text{O}_7$ NP while the peaks at higher potential are attributed to the PA/ Ti_3O_7 NS. The latter is consistent with prior results for Na-ion insertion into $\text{Na}_{1-x}\text{H}_x\text{Ti}_3\text{O}_7$ solid solution.⁴⁸ The development of these peaks produces a corresponding capacity increase from 95 to 125 mAh g^{-1} , which stabilizes after 10 cycles (Figure S17). The reason for this capacity increase arises from ion-exchange between Na^+ in the electrolyte and PA^+ ions still present in $\text{Na}_2\text{Ti}_3\text{O}_7$ NP-NS. This ion-exchange mechanism during electrochemical cycling is typical of nanosheets where bulkier positively charged cations are exchanged for smaller sized cations with a parallel increase in capacity.⁴⁹ It takes several cycles to exchange Na^+ in the electrolyte for the larger PA^+ ions remaining from the complex synthesis. Once this occurs, constant Na-ion insertion coupled with a stable SEI formation leads to coulombic efficiencies above 95%. The first cycle does not show redox peaks at low potentials (< 0.5 V) since the PA^+ needs to be exchanged for Na^+ before the Na^+ can be fully intercalated. For the experiments carried out with nearly pure $\text{Na}_2\text{Ti}_3\text{O}_7$ NP (low concentration of nanosheets), redox peaks at low potentials are barely detectable for the first cycle (Figure S18a). By the second cycle, the redox peaks for Na-ion insertion into the nanoplatelets are observed for both $\text{Na}_2\text{Ti}_3\text{O}_7$ NP-NS and $\text{Na}_2\text{Ti}_3\text{O}_7$ NP (Figure S18b). The intensity of these peaks continues to increase with cycling.

Ex-situ XPS was used to investigate the ion-exchange process occurring in the $\text{Na}_2\text{Ti}_3\text{O}_7$ NP-NS by determining the ratio between the Na 1s and N 1s peaks before and after electrochemical cycling. Before cycling, there is an intense N 1s signal and a weaker Na 1s signal as shown in Figures 6b,c, respectively. After several cycles, a strong Na 1s signal now appears and although the signal-to-noise ratio is high, there still exists a slight N 1s peak, indicating that a small amount of PA^+ is retained after cycling. As indicated in Table S2, the Na^+ content after cycling increases from 0.5% to 6.1% and the $-\text{C}-\text{NH}_3^+$ content decreases from 3.3% to 0.6%. Also, there is a slight shift (+0.6 eV) of the Na 1s peak from 1071 to 1071.6 eV. This change in binding energy for Na was observed previously and was proposed to be associated with SEI formation.⁵⁰

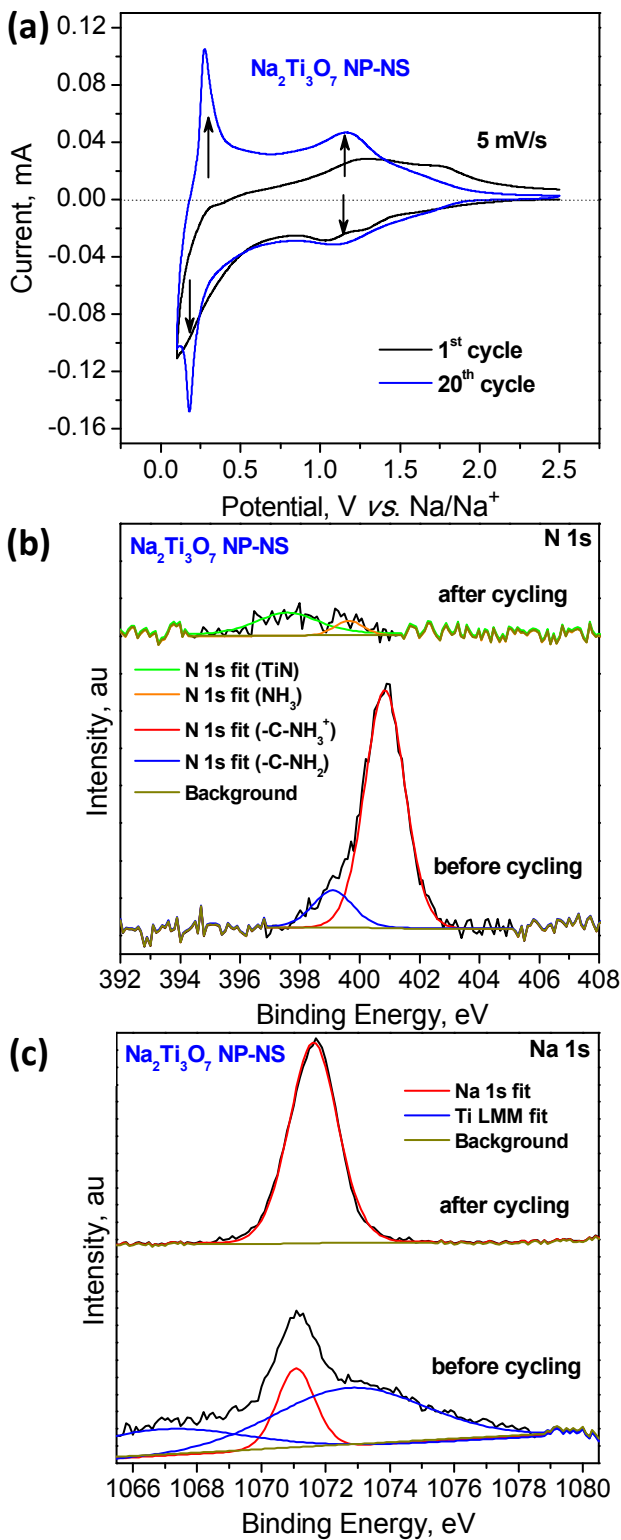


Figure 6. (a) Cyclic voltammogram of 1st and 20th cycle for mixed nanoplatelets and nanosheets of Na₂Ti₃O₇ cycled at 5 mV s⁻¹. X-ray photoelectron spectra of mixed nanoplatelets and nanosheets of Na₂Ti₃O₇ from the (b) N 1s and (c) Na 1s core-levels before and after electrochemical cycling.

CONCLUSIONS

The sodium charge storage properties of $\text{Na}_2\text{Ti}_3\text{O}_7$, a promising negative electrode for sodium-ion batteries are compromised by the slow kinetics and poor cycling behavior of the bulk material. In this study, we considered whether exfoliated $\text{Na}_2\text{Ti}_3\text{O}_7$ could overcome these limitations as charge storage would occur on the surface or within a few layers. The liquid phase exfoliation method developed here produced both nanosheets and nanoplatelets that undergo redox reactions upon Na-ion insertion. The electrochemical properties benefitted from the ion exchange processes that occurred during the initial electrochemical cycling. The charge storage kinetics for the nanosheets is capacitor-like in nature while that of the nanoplatelets is diffusion-controlled and resembles that of bulk $\text{Na}_2\text{Ti}_3\text{O}_7$. Materials that combined both nanosheets and nanoplatelets exhibited far better charge storage properties (110 mAh g^{-1} at 10C) and stable cycling behavior than that of the corresponding bulk materials, underscoring the importance of the 2D nanoscale morphology.

ASSOCIATED CONTENT

Supporting Information

The supporting information is available free of charge on the ACS Publications website at DOI:

Sample preparation for structural and electrochemical characterization; EDX spectra and XRD patterns of proton exchanged $[\text{H}_x\text{Na}_{2-x}]\text{Ti}_3\text{O}_7$; Illustration of differential centrifugation process for obtaining control samples of nanoplatelets and nanosheets; XRD patterns and CVs for the control samples of nanoplatelets and nanosheets; AFM images of PA/ Ti_3O_7 NS; Estimation of the number of layers of the control samples using XRD; Total X-ray scattering measurements for bulk $\text{Na}_2\text{Ti}_3\text{O}_7$ and $\text{Na}_2\text{Ti}_3\text{O}_7$ NP-NS; Azimuthal scan of $\text{Na}_2\text{Ti}_3\text{O}_7$ NP-NS showing morphological anisotropy; XPS survey scans, high resolution fittings, and table summarizing the atomic percentages of Na 1s, N 1s, Ti 2p, and O 1s for bulk $\text{Na}_2\text{Ti}_3\text{O}_7$, PA/ Ti_3O_7 NS, $\text{Na}_2\text{Ti}_3\text{O}_7$ NP-NS, and estimated actual composition for $\text{Na}_2\text{Ti}_3\text{O}_7$, PA/ Ti_3O_7 NS, $\text{Na}_2\text{Ti}_3\text{O}_7$ NP-NS, and $\text{Na}_2\text{Ti}_3\text{O}_7$ NP-NS after cycling in a non-aqueous Na-ion electrolyte; cyclic voltammograms of $\text{Na}_2\text{Ti}_3\text{O}_7$ NP-NS swept from $1 - 20 \text{ mV s}^{-1}$; *b*-value extrapolation from $1 - 20 \text{ mV s}^{-1}$ for both $\text{Na}_2\text{Ti}_3\text{O}_7$ NP and PA/ Ti_3O_7 NS control samples; galvanostatic discharge curve showing the irreversible capacity on the 1st cycle associated with SEI formation; long-term cycling for $\text{Na}_2\text{Ti}_3\text{O}_7$ NP-NS cycled at 10C for 1000 cycles; derivative dQ/dV plots of $\text{Na}_2\text{Ti}_3\text{O}_7$ nanoplatelets-nanosheets mixture at 5C and 20C; Electrochemical data on standard electrodes prepared with exfoliated $\text{Na}_2\text{Ti}_3\text{O}_7$ NP-NS (1 mg cm^{-2} loading) to complement results with drop cast electrodes ($40 \text{ } \mu\text{g cm}^{-2}$ loading); capacity vs. cycle number showing stable capacities after 10 cycles for $\text{Na}_2\text{Ti}_3\text{O}_7$ NP-NS; 1st and 2nd cycle cyclic voltammograms of $\text{Na}_2\text{Ti}_3\text{O}_7$ NP and $\text{Na}_2\text{Ti}_3\text{O}_7$ NP-NS

AUTHOR INFORMATION

Corresponding Author

*Bruce Dunn. Email: bdunn@ucla.edu

Notes

The authors declare no competing financial interests.

ACKNOWLEDGMENTS

This work was supported as part of the Navy Undersea Research Program (N00014-13-1-0605) and also funded by the Office of Naval Research (N00014-16-1-2164). The authors would like to thank Dr. Jeffrey Long of the U.S. Naval Research Laboratory for the continual support in providing constructive feedback for this project. This research used resources of the Advanced Photon Source, a U.S. Department of Energy (DOE) Office of Science User Facility operated for the DOE Office of Science by Argonne National Laboratory under Contract No. DE-AC02-06CH11357. X-ray scattering experiments were performed at APS 11-ID-B under GUP-45245. VDN is supported by the University of California President's Postdoctoral Fellowship and the University of California, Santa Barbara California NanoSystems Institute Elings Prize Fellowship.

REFERENCES

- (1) Dunn, B.; Kamath, H.; Tarascon, J.-M. Electrical Energy Storage for the Grid: A Battery of Choices. *Science* **2011**, *334*, 928–935.
- (2) Yang, Z.; Zhang, J.; Kintner-Meyer, M. C. W.; Lu, X.; Choi, D.; Lemmon, J. P. Electrochemical Energy Storage for Green Grid. *Chem. Rev.* **2011**, *111*, 3577–3613.
- (3) Slater, M. D.; Kim, D.; Lee, E.; Johnson, C. S. Sodium-Ion Batteries. *Adv. Funct. Mater.* **2013**, *23*, 947–958.
- (4) Palomares, V.; Serras, P.; Villaluenga, I.; Hueso, K. B.; Carretero-González, J.; Rojo, T. Na-Ion Batteries, Recent Advances and Present Challenges to Become Low Cost Energy Storage Systems. *Energy Environ. Sci.* **2012**, *5*, 5884–5901.
- (5) Palomares, V.; Casas-Cabanas, M.; Castillo-Martínez, E.; Han, M. H.; Rojo, T. Update on Na-Based Battery Materials. A Growing Research Path. *Energy Environ. Sci.* **2013**, *6*, 2312–2337.
- (6) Kim, S. W.; Seo, D. H.; Ma, X.; Ceder, G.; Kang, K. Electrode Materials for Rechargeable Sodium-Ion Batteries: Potential Alternatives to Current Lithium-Ion Batteries. *Adv. Energy Mater.* **2012**, *2*, 710–721.
- (7) Larcher, D.; Tarascon, J.-M. Towards Greener and More Sustainable Batteries for Electrical Energy Storage. *Nat. Chem.* **2015**, *7*, 19–29.
- (8) Yabuuchi, N.; Kubota, K.; Dahbi, M.; Komaba, S. Research Development on Sodium-Ion Batteries. *Chem. Rev.* **2014**, *114*, 11636–11682.
- (9) Dahbi, M.; Yabuuchi, N.; Kubota, K.; Tokiwa, K.; Komaba, S. Negative Electrodes for Na-

Ion Batteries. *Phys. Chem. Chem. Phys.* **2014**, *16*, 15007–15028.

(10) Doeff, M. M.; Cabana, J.; Shirpour, M. Titanate Anodes for Sodium Ion Batteries. *J. Inorg. Organomet. Polym. Mater.* **2014**, *24*, 5–14.

(11) Shirpour, M.; Cabana, J.; Doeff, M. New Materials Based on a Layered Sodium Titanate for Dual Electrochemical Na and Li Intercalation Systems. *Energy Environ. Sci.* **2013**, *6*, 2538–2547.

(12) Shirpour, M.; Cabana, J.; Doeff, M. Lepidocrocite-Type Layered Titanate Structures: New Lithium and Sodium Ion Intercalation Anode Materials. *Chem. Mater.* **2014**, *26*, 2502–2512.

(13) Senguttuvan, P.; Rousse, G.; Seznec, V.; Tarascon, J. M.; Palacín, M. R. Na₂Ti₃O₇: Lowest Voltage Ever Reported Oxide Insertion Electrode for Sodium Ion Batteries. *Chem. Mater.* **2011**, *23*, 4109–4111.

(14) Rudola, A.; Saravanan, K.; Mason, C. W.; Balaya, P. Na₂Ti₃O₇: An Intercalation Based Anode for Sodium-Ion Battery Applications. *J. Mater. Chem. A* **2013**, *1*, 2653–2662.

(15) Senguttuvan, P.; Rousse, G.; Seznec, V.; Tarascon, J.-M.; Palacín, M. R. Na₂Ti₃O₇. *Chem. Mater.* **2011**, *23*, 4109–4111.

(16) Pan, H.; Lu, X.; Yu, X.; Hu, Y.-S.; Li, H.; Yang, X.-Q.; Chen, L. Sodium Storage and Transport Properties in Layered Na₂Ti₃O₇ for Room-Temperature Sodium-Ion Batteries. *Adv. Energy Mater.* **2013**, *3*, 1186–1194.

(17) Rousse, G.; Dompablo, M. E. A.; Senguttuvan, P.; Ponrouch, A.; Tarascon, J.-M.; Palacín, M. R. Rationalization of Intercalation Potential and Redox Mechanism for A₂Ti₃O₇ (A = Li, Na). *Chem. Mater.* **2013**, *25*, 4946–4956.

(18) Geim, A. K.; Novoselov, K. S. The Rise of Graphene. *Nat. Mater.* **2007**, *6*, 183–191.

(19) Ma, R.; Sasaki, T. Nanosheets of Oxides and Hydroxides: Ultimate 2D Charge-Bearing Functional Crystallites. *Adv. Mater.* **2010**, *22*, 5082–5104.

(20) Coleman, J. N.; Lotya, M.; O'Neill, A.; Bergin, S. D.; King, P. J.; Khan, U.; Young, K.; Gaucher, A.; De, S.; Smith, R. J.; Shvets, I. V.; Arora, S. K.; Stanton, G.; Kim, H.-Y.; Lee, K.; Kim, G. T.; Duesberg, G. S.; Hallam, T.; Boland, J. J.; Wang, J. J.; Donegan, J. F.; Grunlan, J. C.; Moriarty, G.; Shmeliov, A.; Nicholls, R. J.; Perkins, J. M.; Grieveson, E. M.; Theuvsen, K.; McComb, D. W.; Nellist, P. D.; Nicolosi, V. Two-Dimensional Nanosheets Produced by Liquid Exfoliation of Layered Materials. *Science* **2011**, *331*, 568–571.

(21) Osada, M.; Sasaki, T. Exfoliated Oxide Nanosheets: New Solution to Nanoelectronics. *J. Mater. Chem.* **2009**, *19*, 2503.

(22) Nicolosi, V.; Chhowalla, M.; Kanatzidis, M. G.; Strano, M. S.; Coleman, J. N. Liquid Exfoliation of Layered Materials. *Science* **2013**, *340*, 1226419-1–18.

(23) Pu, J.; Yomogida, Y.; Liu, K.-K.; Li, L.-J.; Iwasa, Y.; Takenobu, T. Highly Flexible MoS₂ Thin-Film Transistors with Ion Gel Dielectrics. *Nano Lett.* **2012**, *12*, 4013–4017.

(24) Liu, K. K.; Zhang, W.; Lee, Y. H.; Lin, Y. C.; Chang, M. T.; Su, C. Y.; Chang, C. S.; Li, H.; Shi, Y.; Zhang, H.; Lai, C. S.; Li, L. J. Growth of Large-Area and Highly Crystalline MoS₂ Thin Layers on Insulating Substrates. *Nano Lett.* **2012**, *12*, 1538–1544.

(25) Lee, Y. H.; Zhang, X. Q.; Zhang, W.; Chang, M. T.; Lin, C. T.; Chang, K. D.; Yu, Y. C.;

Wang, J. T.; Chang, C. S.; Li, L. J.; Lin, T. W. Synthesis of Large-Area MoS₂ Atomic Layers with Chemical Vapor Deposition. *Adv. Mater.* **2012**, *24*, 2320–2325.

(26) Chupas, P. J.; Qiu, X.; Hanson, J. C.; Lee, P. L.; Grey, C. P.; Billinge, S. J. L. Rapid-Acquisition Pair Distribution Function (RA-PDF) Analysis. *J. Appl. Crystallogr.* **2003**, *36*, 1342–1347.

(27) Ilavsky, J. Nika: Software for Two-Dimensional Data Reduction. *J. Appl. Crystallogr.* **2012**, *45*, 324–328.

(28) Hammersley, A. P.; Svensson, S. O.; Hanfland, M.; Fitch, A. N.; Hausermann, D. Two-Dimensional Detector Software: From Real Detector to Idealised Image or Two-Theta Scan. *High Press. Res.* **1996**, *14*, 235–248.

(29) Qiu, X.; Thompson, J. W.; Billinge, S. J. L. PDFgetX2: A GUI Driven Program to Obtain the Pair Distribution Function from X-Ray Powder Diffraction Data. *J. Appl. Crystallogr.* **2004**, *37*, 678–678.

(30) Augustyn, V.; Come, J.; Lowe, M. A.; Kim, J. W.; Taberna, P.-L.; Tolbert, S. H.; Abruña, H. D.; Simon, P.; Dunn, B. High-Rate Electrochemical Energy Storage through Li⁺ Intercalation Pseudocapacitance. *Nat. Mater.* **2013**, *12*, 518–522.

(31) Miyamoto, N.; Kuroda, K.; Ogawa, M. Exfoliation and Film Preparation of a Layered Titanate, Na₂Ti₃O₇, and Intercalation of Pseudoisocyanine Dye. *J. Mater. Chem.* **2004**, *14*, 165–170.

(32) Kikkawa, S.; Koizumi, M. Organic Intercalation on Layered Compound KTiNbO₅. *Mater. Res. Bull.* **1980**, *15*, 533–539.

(33) Miyamoto, N.; Kuroda, K.; Ogawa, M. Aggregation of a Cationic Cyanine Dye Intercalated in the Interlayer Space of a Layered Titanate Na₂Ti₃O₇. *Mol. Cryst. Liq. Cryst. Sci. Technol. Sect. A. Mol. Cryst. Liq. Cryst.* **2000**, *341*, 259–264.

(34) Livshits, M. A.; Khomyakova, E.; Evtushenko, E. G.; Lazarev, V. N.; Kulemin, N. A.; Semina, S. E.; Generozov, E. V.; Govorun, V. M. Isolation of Exosomes by Differential Centrifugation: Theoretical Analysis of a Commonly Used Protocol. *Sci. Rep.* **2015**, *5*, 17319.

(35) Andersson, S.; Wadsley, A. D. The Crystal Structure of Na₂Ti₃O₇. *Acta Crystallogr.* **1961**, *14*, 1245–1249.

(36) Zhang, Z.; Goodall, J. B. M.; Brown, S.; Karlsson, L.; Clark, R. J. H.; Hutchison, J. L.; Rehman, I. U.; Darr, J. a. Continuous Hydrothermal Synthesis of Extensive 2D Sodium Titanate (Na₂Ti₃O₇) Nano-Sheets. *Dalt. Trans.* **2010**, *39*, 711–714.

(37) Muller, G. A.; Cook, J. B.; Kim, H.-S.; Tolbert, S. H.; Dunn, B. High Performance Pseudocapacitor Based on 2D Layered Metal Chalcogenide Nanocrystals. *Nano Lett.* **2015**, *15*, 1911–1917.

(38) Doan-Nguyen, V. V. T.; Kimber, S. A. J.; Pontoni, D.; Reifsnnyder Hickey, D.; Diroll, B. T.; Yang, X.; Miglierini, M.; Murray, C. B.; Billinge, S. J. L. Bulk Metallic Glass-like Scattering Signal in Small Metallic Nanoparticles. *ACS Nano* **2014**, *8*, 6163–6170.

(39) Kerber, S. J. The Nature of Hydrogen in X-Ray Photoelectron Spectroscopy: General Patterns from Hydroxides to Hydrogen Bonding. *J. Vac. Sci. Technol. A Vacuum, Surfaces, Film.*

1996, 14, 1314.

(40) Strother, T.; Hamers, R. J.; Smith, L. M. Covalent Attachment of Oligodeoxyribonucleotides to Amine-Modified Si (001) Surfaces. *Nucleic Acids Res.* **2000**, 28, 3535–3541.

(41) Rignanese, G.; Pasquarello, A.; Charlier, J.; Gonze, X.; Car, R. Nitrogen Incorporation at Si(001)-SiO₂ Interfaces : Relation between N 1s Core-Level Shifts and Microscopic Structure. *Phys. Rev. Lett.* **1997**, 79, 5174–5177.

(42) Kowalczyk, S. P.; Ley, L.; McFeely, F. R.; Pollak, R. A.; Shirley, D. A. X-Ray Photoemission from Sodium and Lithium. *Phys. Rev. B* **1973**, 8, 3583–3585.

(43) Xu, J.; Ma, C.; Balasubramanian, M.; Shirley, Y. Understanding Na₂Ti₃O₇ as an Ultra-Low Voltage Anode Material for a Na-Ion Battery. *Chem. Commun.* **2014**, 50, 12564–12567.

(44) Augustyn, V.; Simon, P.; Dunn, B. Pseudocapacitive Oxide Materials for High-Rate Electrochemical Energy Storage. *Energy Environ. Sci.* **2014**, 7, 1597–1614.

(45) Okubo, M.; Hosono, E.; Kim, J.; Enomoto, M.; Kojima, N.; Kudo, T.; Zhou, H.; Honma, I. Nanosize Effect on High-Rate Li-Ion Intercalation in LiCoO₂ Electrode. *J. Am. Chem. Soc.* **2007**, 129, 7444–7452.

(46) Lindström, H.; Södergren, S.; Solbrand, A.; Rensmo, H.; Hjelm, J.; Hagfeldt, A.; Lindquist, S.-E. Li⁺ Ion Insertion in TiO₂ (Anatase). 2. Voltammetry on Nanoporous Films. *J. Phys. Chem. B* **1997**, 101, 7717–7722.

(47) Liu, T.-C.; Pell, W. G.; Conway, B. E. Behavior of Molybdenum Nitrides as Materials for Electrochemical Capacitors. *J. Electrochem. Soc.* **1998**, 145, 1882–1888.

(48) Eguía-Barrio, A.; Castillo-Martinez, E.; Zarrabeitia, M.; Muñoz-Márquez, M. A.; Casas-Cabanas, M.; Rojo, T. Structure of H₂Ti₃O₇ and Its Evolution during Sodium Insertion as Anode for Na Ion Batteries. *Phys. Chem. Chem. Phys.* **2015**, 17, 6988–6994.

(49) Augustyn, V.; White, E. R.; Ko, J.; Grüner, G.; Regan, B. C.; Dunn, B. Lithium-Ion Storage Properties of Titanium Oxide Nanosheets. *Mater. Horizons* **2014**, 1, 219–223.

(50) Muñoz-Márquez, M. A.; Zarrabeitia, M.; Castillo-Martínez, E.; Eguía-Barrio, A.; Rojo, T.; Casas-Cabanas, M. Composition and Evolution of the Solid-Electrolyte Interphase in Na₂Ti₃O₇ Electrodes for Na-Ion Batteries: XPS and Auger Parameter Analysis. *ACS Appl. Mater. Interfaces* **2015**, 7, 7801–7808.

TOC Image

